Journal of Power Sources 681 (2026) 240276

Contents lists available at ScienceDirect

Journal of Power Sources

journal homepage: www.elsevier.com/locate/jpowsour

Characterization of the grain boundary strength of polycrystalline NMC811 using in situ micro tensile tests

Tobias Sedlatschek [a,b,*], Leonhard Gertlowski [a,b], Felix Weber [b], Christoph Broeckmann [a,b]

[a] Institute for Materials Applications in Mechanical Engineering, RWTH Aachen University, Augustinerbach 4 52062 Aachen, Germany
[b] Institute of Applied Powder Metallurgy and Ceramics at RWTH Aachen e.V., Augustinerbach 4 52062 Aachen, Germany

HIGHLIGHTS

- An optimized push-to-pull geometry for micro tensile testing was developed.
- The grain boundary strength and stiffness were determined for NMC811.
- The fracture behavior of NMC811 was examined.

ARTICLE INFO

Keywords:
Nickel rich cathode
Particle compression
Interface characterization
Geometry optimization
Finite element simulation

ABSTRACT

$LiNi_xCo_yMn_{1-x-y}O_2$ (NMC) is one of the most relevant lithium-ion battery cathode materials. In this study, micromechanical tests were used to examine the fracture behavior of $LiNi_{0.8}Co_{0.1}Mn_{0.1}O_2$ (NMC811) secondary particles. Furthermore, the grain boundary strength was measured and the grain boundary stiffness was estimated to 521 GPa μm^{-1}. Using an optimized push-to-pull sample geometry produced by focused ion beam (FIB) technology and measuring the displacement through digital image correlation (DIC), micro tensile tests were performed and validated against nanoindentation. A Weibull distribution characteristic tensile strength of 745 MPa followed by a brittle fracture behavior was measured. The fracture surface was examined and showed an intercrystalline fracture. Through electron backscatter diffraction (EBSD) analysis, less frequently occurring transcrystalline fracture was detected. Scanning transmission electron microscopy (STEM) showed a slight increase in dislocation density within the testing section in comparison to reference positions. The results can be used for a more detailed understanding of the mechanical degradation during the cycling of batteries as well as for building accurate simulation models.

1. Introduction

With batteries playing an increasingly important role in daily life, the focus is on the durability of batteries. One reason for capacity loss in batteries based on NMC811 cathodes is the formation of reaction layers on fresh surface which is exposed to the liquid electrolyte after particle cracking [1]. Furthermore, the separation of some regions from the remaining active material through cracking also contributes to a reduced cycle life. The two mechanisms also lead to an increased cell impedance which results in a reduced rate capability. To better understand this cracking phenomenon and to improve the longevity of batteries, a profound understanding of the mechanical properties and the fracture behavior is crucial. In this context, interfaces and in particular grain boundaries play a key role since crack propagation along the grain boundaries is commonly observed during electrochemical cycling [2]. Therefore, the grain boundary properties must be investigated.

Interface properties can be investigated in micromechanical experiments such as micro cantilever bending tests [3,4] or micro tensile tests. Two methods for micro tensile tests are established: direct-pull tests (Fig. 1(a)) and push-to-pull tests. While the former are more intuitive and closer to macroscopic tensile tests in terms of sample geometry, they require specialized testing equipment and pose challenges in terms of gripping and sample alignment.

On the other hand, push-to-pull tests can be conducted in any nanoindenter. There are two subgroups of push-to-pull tests: ones where the sample is applied to a dedicated push-to-pull device and ones where the push-to-pull geometry is directly produced from the sample itself. While the former subgroup is well-established for 1D and 2D

* Corresponding author at: Institute for Materials Applications in Mechanical Engineering, RWTH Aachen University, Augustinerbach 4 52062 Aachen, Germany.
E-mail addresses: t.sedlatschek@iwm.rwth-aachen.de (T. Sedlatschek), l.gertlowski@iwm.rwth-aachen.de (L. Gertlowski), f.weber@iwm.rwth-aachen.de (F. Weber), c.broeckmann@iwm.rwth-aachen.de (C. Broeckmann).

https://doi.org/10.1016/j.jpowsour.2026.240276
Received 20 January 2026; Received in revised form 15 April 2026; Accepted 28 April 2026
Available online 8 May 2026
0378-7753/© 2026 The Authors. Published by Elsevier B.V. This is an open access article under the CC BY license (http://creativecommons.org/licenses/by/4.0/).

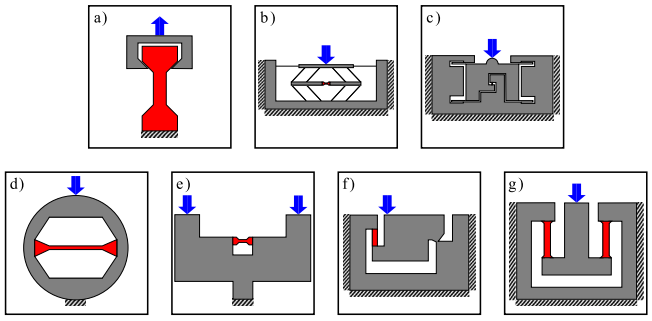


Fig. 1. Schematic representation of different methods for micro tensile tests: (a) direct-pull test, (b) dedicated push-to-pull device by Ganesan et al. [5,6], (c) dedicated push-to-pull device by Hysitron Incorporated [7], (d) integrated push-to-pull design by Durelli et al. [8] and Quinn et al. [9], (e) integrated push-to-pull design by Ding et al. [10], (f) integrated push-to-pull design by Kiener et al. [11], (g) integrated push-to-pull design by Schwiedrzik et al. [12].

materials, the latter has the advantage of complete flexibility in terms of sample design including thick sections.

Two dedicated push-to-pull devices are established: The first design was introduced by Ganesan et al. [5,6] (Fig. 1(b)). For this device, additive manufacturing was demonstrated as an alternative fabrication method [13]. The second geometry was developed by Hysitron Incorporated [7] (Fig. 1(c)). Both devices remain extensively used until today [14,15].

An alternative geometry with an integrated push-to-pull frame – the theta specimen – was originally introduced in 1962 by Durelli at al. [8] and was miniaturized by Quinn et al. [9] (Fig. 1(d)). Different fabrication methods such as lithography [16], FIB milling [17] and most recently additive manufacturing [18,19] were used to produce the samples. A similar approach was introduced by Ding et al. [10], who used on open C-shaped geometry instead of the closed theta-like geometry (Fig. 1(e)). However, no direct force measurement in the testing section is possible with these sample geometries because the applied force is distributed onto the sample frame and the testing section. Furthermore, the displacement measurement is challenging because the displacement in the testing section does not equal the applied displacement. One way to measure the displacement in the testing section is the use of DIC based on high resolution scanning electron microscopy (SEM) images taken during the test. This method can be used to build a virtual extensometer or to measure displacement fields [20].

Kiener et al. [11] introduced an asymmetric fully FIB produced push-to-pull geometry for micro tensile tests (Fig. 1(f)), but the stress state and the influence of the hinge were not investigated. Schwiedrzik et al. [12] simulated and realized a symmetric push-to-pull geometry for fracture toughness measurement — however, their geometry did not result in a homogeneous stress state throughout the entire testing section (Fig. 1(g)). Nevertheless, all these geometries present viable approaches to determine the mechanical properties under tensile load on a microscale. While the measurement of the fracture stress is straight forward, the derivation of the grain boundary stiffness, which generally is a tensor [21] and depends on the misorientation between the grains, requires more attention. To the knowledge of the authors, currently no grain boundary stiffness and strength data for NMC under uniaxial tensile load is available.

Min and Cho [22] determined the in-plane and the out-of-plane anisotropic Young's moduli of the NMC811 crystal using first principles calculations to be 249 GPa and 210 GPa, respectively. The values were confirmed experimentally by Sharma et al. [23] by nanoindentation on NMC811 pellets, where a modulus of 230 GPa was found. These values are higher than the ones calculated by Sun and Zhao [24], He et al. [25] and Liu et al. [26]. They found moduli as low as 168 GPa. Experimentally measured moduli on polycrystalline secondary particles are even lower. Vasconcelos et al. [27,28] and Xu et al. [29] measured 113 GPa, 139 GPa and 143 GPa in NMC532, respectively. Furthermore, they measured indentation hardnesses of 7.8 GPa, 8.9 GPa and 8.6 GPa. The indentation hardness of NMC811 pellets was found to be 14.2 GPa [23]. Although for ceramic-like materials the tensile strength σ_{UTS} equals the yield strength σ_Y, the hardness H of ceramic-like materials cannot be used to estimate the tensile strength using simple correlations such as $\sigma_{UTS} = \sigma_Y = H/3$ [30], hence other experiments are necessary to determine the tensile properties.

The indentation toughness of NMC811 was measured through the analysis of pop-in events in indentation load–displacement curves to $0.271\,\mathrm{MPa}\sqrt{\mathrm{m}}$ [23] which is in good agreement with an estimation made by Stallard et al. [30].

In addition, secondary particles were tested in an assembly similar to a Brazilian test [31–39]. Dang et al. [32] and Wheatcroft et al. [38] found mean fracture tensile strengths of 188 MPa for polycrystalline NMC111 and 207 MPa for polycrystalline NMC811, respectively. Han et al. [39] found fracture strengths between 172.8 MPa and 210.6 MPa for different NMC811 microstructures. However, their results are not directly comparable to a homogeneous uniaxial tensile stress state on the level of the grain boundaries. Hence, the tensile strength of NMC is currently missing. However, the mechanical properties of NMC are highly relevant for the development of simulation models that allow for the optimization of the microstructure with respect to the mechanical integrity of the secondary particles.

In this work, the qualitative fracture behavior under compressive and tensile load as well as the quantitative mechanical properties of NMC811 under crack initiating tensile load are investigated. For this purpose, an optimized push-to-pull sample geometry which allows for tensile testing with a homogeneous uniaxial stress state is developed. The displacement is measured using DIC. The data allows for a better understanding of the mechanical degradation of battery materials and provides an experimental base for simulation models.

2. Material and methods

2.1. Material

In this study, a commercial NMC811 electrode was investigated. The sample was argon ion polished using a Jeol SM-09010 Cross Section Polisher to allow for nanoindentation and EBSD examinations. An overview of the microstructure is provided in Fig. 2(a). The electrode consists of nearly spherical secondary particles with diameters smaller than ≈19 µm (99 percentile of a fitted lognormal distribution) with most secondary particles having diameters smaller than ≈10 µm (80 percentile of a fitted lognormal distribution). The dimensions were measured from SEM images taken in a Tescan Clara SEM. The secondary particles are composed of single crystalline primary particles (grains) with diameter and standard deviation of 598 ± 305 nm measured using EBSD. The EBSD measurements were performed in an FEI Helios NanoLab G3 CX FIB-SEM.

The formation of reaction layers on the sample surface was avoided by minimizing sample transfer times between the Cross Section Polisher and the SEMs.

2.2. Compression fracture tests

In order to qualitatively assess the fracture behavior of the secondary particles under compressive load, a simple fracture test was employed. Therefore, the cross-section of secondary particles was polished using the FEI Helios NanoLab G3 CX FIB-SEM. The Tescan Clara SEM equipped with a Bruker Hysitron PI 89 SEM PicoIndenter with a flat punch indenter tip (diameter 5 µm) was used to apply a compressive load on the secondary particle (see Fig. 2(b)) while observing the polished cross-section in real time. The maximum displacement was set to 5 µm and the loading time to 15 s. A video of the test was recorded. During the test, the secondary particles are held in place by the polymeric binder already present in the electrode.

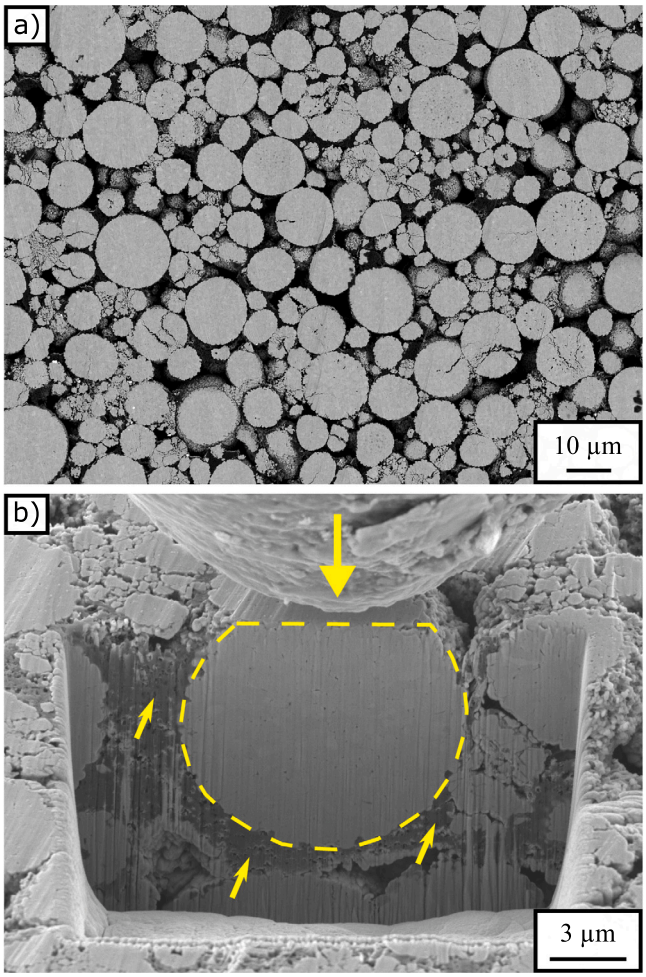


Fig. 2. (a) Backscattered electron image of the ion polished NMC811 sample and (b) FIB-polished cross-section of an exemplary secondary particle (dashed line) with the flat punch indenter tip and the loading direction (large arrow) above the secondary particle. Several binder regions are indicated exemplarily with small arrows. The primary particles are visible as faint brightness differences on the cross-section.

2.3. Sample geometry optimization

The push-to-pull sample geometry suggested by Kiener et al. [11] is an approach for performing micro tensile tests in regular nanoindenters which does not require the use of prefabricated push-to-pull devices. However, through its asymmetric nature, bending moments are introduced into the testing section which results in a non-homogeneous and non-uniaxial stress state. Therefore, the sample geometry was optimized in order to achieve a homogeneous and uniaxial stress state in the testing section. For this purpose, finite element simulations were performed.

A 2.5D model (i.e. a planar model with a small thickness) using linear hexahedral elements with reduced integration was developed in Abaqus. Due to the expected brittle fracture behavior, a linear-elastic material model was used. A Young's modulus of 138 GPa measured by nanoindentation was used in the model and the deformation condition at a hypothetical stress of 1000 MPa in the testing section was analyzed. Fixed boundary conditions on the one side and a hinge realized through a kinematic coupling between the sample geometry and a constraint reference point on the other side were established, see Fig. 3. Since the load is applied using a spherical indenter tip in the experiment, the load in the simulation model is applied on a circular segment.

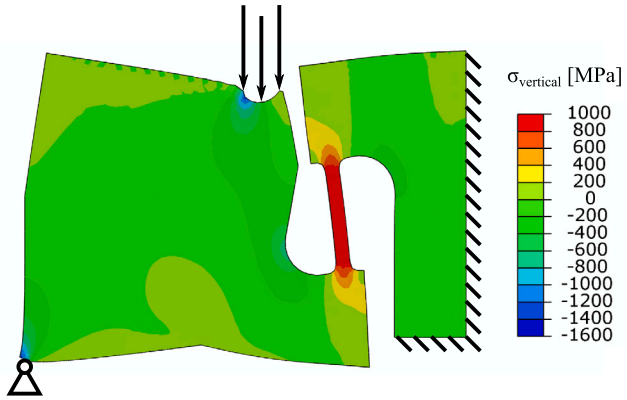


Fig. 3. Homogeneous and uniaxial stress state in vertical direction in the testing section of the optimized sample geometry deformed under the acting load. A deformation scale factor of 20 was applied.

The stiffnesses of the arm below and the arm above the testing section were matched through changes in their shape in order to achieve deformations in these arms eliminating the bending moments. The resulting deformed sample geometry and the stress state are shown in Fig. 3. For visualization purposes, the deformations were scaled by a factor of 20. During the micro tensile tests, the sample deformation and rotation is very small resulting in a uniaxial loading in the testing section. The deviation between the maximum stress in vertical direction on one edge of the testing section and the minimum stress in vertical direction on the opposite edge of the testing section is 3.7 %. The undeformed sample geometry can be found in Supplementary material 1.

2.4. Micro tensile tests using DIC

The samples for the micro tensile tests were produced in the FEI Helios NanoLab G3 CX FIB-SEM. Large and defect-free particles were chosen for the tests. Locations at which defects became visible during the production of the micro tensile test samples were discarded. The dimensions of the rectangular testing section were approximately 2.7 µm (length), 500 nm (width) and 1.3 µm (thickness). The exact dimensions were measured for each sample to calculate the respective stress–strain curves. Two platinum points were sputtered on the surface of the testing section to measure the displacement through digital image correlation [20]. The points were placed at the upper and lower end of the testing section. The relative motion of the points was analyzed using ImageJ [40] to derive the displacement and the strain in the testing section. A Savitzky–Golay filter was applied on the displacement data to reduce the noise. The load in the testing section F_{TS} was calculated through a moment equilibrium equation based on the measured force $F_{Indenter}$ and the measured horizontal lever arms between the hinge and the force application point $d_{Hinge-Tip}$ and the hinge and the testing section $d_{Hinge-TS}$ and did not require any post processing.

$$F_{TS} = F_{Indenter} \cdot \frac{d_{Hinge-Tip}}{d_{Hinge-TS}} \tag{1}$$

The micro tensile tests were performed in the Tescan Clara SEM equipped with a Bruker Hysitron PI 89 SEM PicoIndenter with a conospherical tip (tip radius 1 µm) provided by Synton MDP (Switzerland). The displacement rate of the nanoindenter was set to 0.37 nm s^{-1}. This value resulted in a strain rate equivalent to a charge rate slightly smaller than 1 C which is a realistic charge/discharge scenario for a battery. During the test, a video was recorded, which was used to evaluate the displacement after the test.

The fractured samples were examined post mortem using SEM and STEM imaging as well as transmission Kikuchi diffraction (TKD).

2.5. Nanoindentation

Targeted nanoindentation was performed as a validation for the micro tensile tests. The Bruker Hysitron PI 89 SEM PicoIndenter equipped with a diamond Berkovich tip provided by Synton MDP (Switzerland) in the Tescan Clara SEM was used. The tip area function was calibrated on a fused silica sample before the tests. Continuous stiffness measurement with an indentation strain rate of $0.2\,s^{-1}$ to a maximum indentation load of 5 mN was used. The Oliver and Pharr Method [41] was employed to calculate the reduced modulus and an extrapolation of the reduced modulus to the surfaces was conducted to correct for a substrate effect [42]. A Poisson's ratio of 0.32 was assumed for NMC [43] to derive the Young's modulus.

3. Results

First, the fracture behavior under compressive loads was examined by observing a cross-section of a secondary particle in a simple compression test. A video of a representative test is available in Supplementary material 2. Intercrystalline fracture was observed, see Fig. 4(a). Furthermore, binder detachment between the secondary particles and the binder occurred. Supplementary material 3 shows a video of a large crack growing from a preexisting small crack. In both cases, the sudden load drop at the moment of crack growth indicates a brittle fracture, see Fig. 4(b). Due to the irregular shape of the cross-sectioned secondary particles, the flexible surrounding and an unknown defect population in their interior, no quantitative results could be derived from these tests.

To confirm the intercrystalline fracture behavior, EBSD measurements were performed on particles showing cracks from the electrode manufacturing process. Spherical indexing in OIM 9 was performed using the master pattern calculated by Wang et al. [44]. A small number of missindexed points was corrected through a pseudosymmetry correction of 90° around the $[0\,\bar{4}\,4\,1]$ axis. It was found that most cracks were following the grain boundaries. However, less frequently, transcrystalline crack growth was detected. In Fig. 5, two grains through which a crack passed are shown. The transcrystalline crack growth can be recognized through regions, in which the crystal has the same orientation on both sides of the crack.

In order to extend the acquired qualitative information about the fracture behavior to quantitative results, micro tensile tests were conducted within the secondary particles. Brittle fracture without prior plastic deformation was observed. A video of a representative test can be found in Supplementary material 4. For visualization purposes, the whole sample is shown. Further tests were done with the field of view only showing the testing section for an increased displacement measurement resolution. The resulting stress–strain curves are shown in Fig. 6(a). Three curves are well-aligned, while one curve differs. This may be due to the pronounced anisotropy of NMC and the small number of grains involved in the test. In the following, this curve is excluded from the analysis. The fracture stresses of the three reliable curves are 840 MPa, 685 MPa and 562 MPa. The Young's moduli are 172 GPa, 168 GPa and 156 GPa, respectively which results in a mean value of 165 GPa and a standard deviation of 7 GPa.

The fracture surfaces were examined post mortem. An example is provided in Fig. 6(b). The individual grains and the intercrystalline fracture can be clearly seen.

Further high-resolution examinations were conducted on the same sample using STEM and TKD techniques, see Figs. 7 and 8. The STEM examinations confirmed that no visible plastic deformation occurred. However, a slightly increased dislocation density was detected in comparison to reference positions outside of the testing section. The slightly increased dislocation density is an indication for a limited plastic deformation of the NMC grains. This aspect is highly relevant for single crystalline NMC, in which plastic deformation is an initiation mechanism for transcrystalline crack growth. Since no before–after

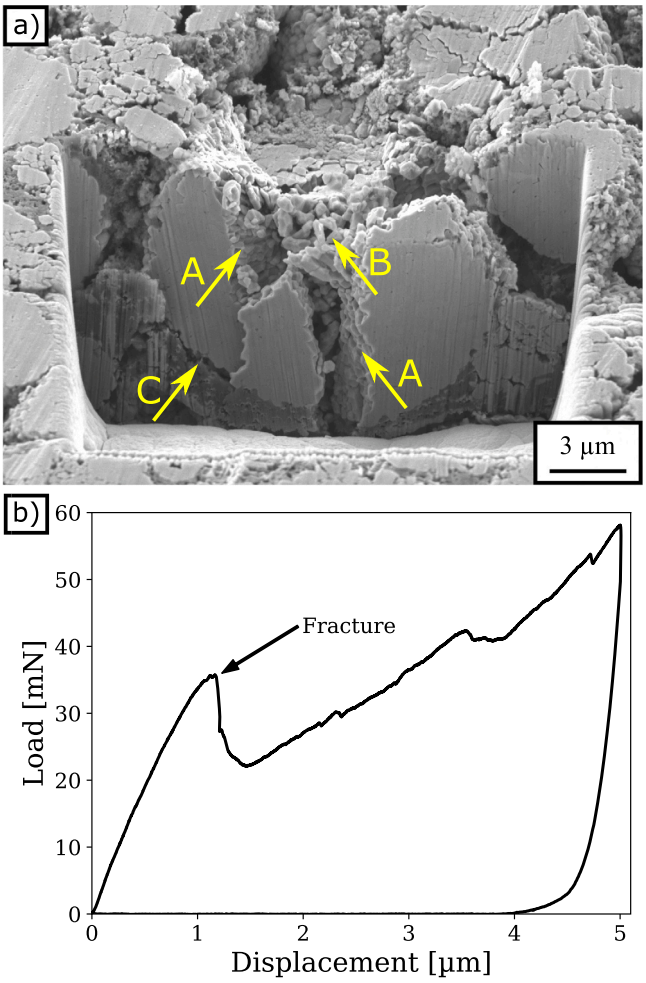


Fig. 4. (a) Fracture of a secondary particle during compression with intercrystalline fracture surfaces (A), individual primary particles (B) as well as binder detachment (C) and (b) corresponding load–displacement curve.

STEM examination of the same location was possible due to a required minimum thickness of the tensile specimen to guarantee a sufficient stability of the geometry, this result should be interpreted with caution. The TKD measurement confirmed the intercrystalline fracture and furthermore no deformation in terms of lattice distortion is visible in the vicinity of the fracture surface and throughout the testing section.

To validate the micro tensile test approach, nanoindentation tests were done. The applied maximum indentation load of 5 mN resulted in indentation depths of approximately 150 nm. The elastically deformed zone that influences the Young's modulus measurement is much larger. Hence, the elastically deformed zone covered several primary particles and the tested volume was comparable to the micro tensile tests. 29 indentations were processed and resulted in a Young's modulus of 138 GPa and a standard deviation of 24 GPa.

4. Discussion

Both in the compression fracture tests and in the micro tensile tests, the material shows a comparable behavior with a brittle fracture. In accordance with the fracture modes observed in the literature during electrochemical cycling, mainly intercrystalline fracture was observed in this study both in compression and in tensile tests. Transcrystalline fracture was found in two grains using EBSD. Within some grains in the testing section of the micro tensile test, dislocations were found, indicating that plastic deformation and material damage within the grains

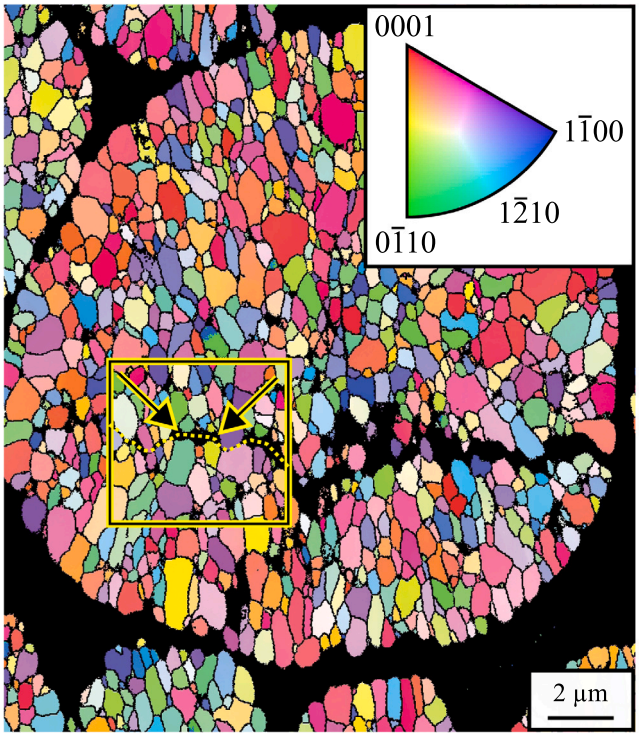


Fig. 5. EBSD of a secondary particle with cracks from the electrode manufacturing process. The crack path in the region of interest is marked with a dotted line and two grains that show transcrystalline fracture are highlighted with arrows.

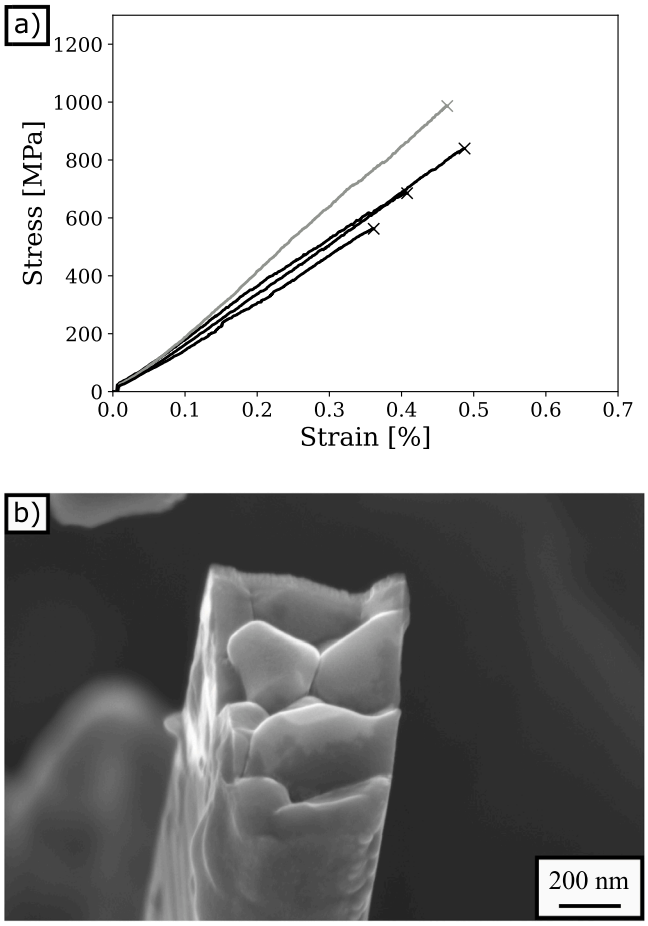


Fig. 6. (a) Stress–strain curves of the micro tensile tests where the light gray curve is an outlier and (b) fracture surface after the micro tensile test.

are possible, but require specific loading conditions to be activated. The compression fracture tests showed binder detachment as an additional damage mechanism. This can decrease the electronic conductivity and therefore increase the impedance.

Assuming a chemical strain during electrochemical cycling due to the expansion/contraction of the unit cell of the order of 10 % [45] and assuming a 1 C charge/discharge, this results in a strain rate of $27.8 \cdot 10^{-6}$ 1/s [46]. The average strain rates during the tensile tests were calculated from the DIC-measured strain at fracture and the time at fracture and amount to $19.4 \cdot 10^{-6}$ 1/s, $24.4 \cdot 10^{-6}$ 1/s and $25.1 \cdot 10^{-6}$ 1/s. This means that the tensile tests correspond to a realistic charge/discharge with charge rates slightly smaller than 1 C. The difference in the strain rates results from small deviations of the sample geometry and the force application point during the experiment. However, all strain rates were in the same order of magnitude.

The Young's modulus measured during the tensile test is comparable to the Young's modulus measured by nanoindentation and also within the range of values measured by other researchers on secondary particles while the modulus of sintered pellets is higher. Furthermore, the standard deviation of 7 GPa shows a good repeatability of the measurement. This demonstrates that the chosen micro tensile test approach is reliable.

The fracture strain of approximately 0.4 % is small in comparison to the expected chemical strains during electrochemical cycling which are of the order of up to 10 % [45]. This results in the fracture of some grain boundaries during an electrochemical cycle. This fracture leads to a stress relief which prevents other grain boundaries from fracturing in the same cycle. In the following cycle however, additional grain boundaries can fail due to a new build-up of stresses. Hence, the mechanical degradation and consequently the capacity loss during the use of lithium-ion batteries is a direct consequence of the mechanical properties of the secondary particles and in particular the grain boundaries.

Based on the three reliable micro tensile tests, a two-parameter Weibull distribution (see cumulative distribution function in Eq. (2)) is fitted to the results. P is the cumulative probability, the characteristic strength σ_{ch} is 745 MPa and the Weibull modulus m is 6.91 using a Maximum Likelihood Estimation.

$$P(\sigma) = 1 - \exp^{-\left(\frac{\sigma}{\sigma_{ch}}\right)^m} \tag{2}$$

Since this characteristic strength is based on the relatively small number of three tests, its reported value is to be interpreted with caution. However, it can serve as a reference value for NMC811 and for comparison with literature data as long as no additional data is available. The Weibull modulus of $m = 6.91$ indicates a high scattering in the data due to the small number of tests.

In comparison to the results from Dang et al. [32], Wheatcroft et al. [38] and Han et al. [39], the characteristic strength measured in this study is about four times higher. This can be explained by the uniaxial stress state in the testing section. The higher triaxiality in the assembly similar to the Brazilian test results in an earlier failure which is also assisted by the rough particle surface. Furthermore, a size effect [47] influences the results. While in the here-presented study, a small volume without large defects was tested, a significantly larger volume with a higher probability for defects is tested when a complete particle is compressed. This shows that in contrast to the particle strength measured by Dang et al. [32], Wheatcroft et al. [38] and Han et al. [39], the micro tensile test approach allowed for the measurement of a strength on the level of the grain boundaries.

Based on the tensile test results, the grain boundary properties can be estimated. Since only a small number of grains was present

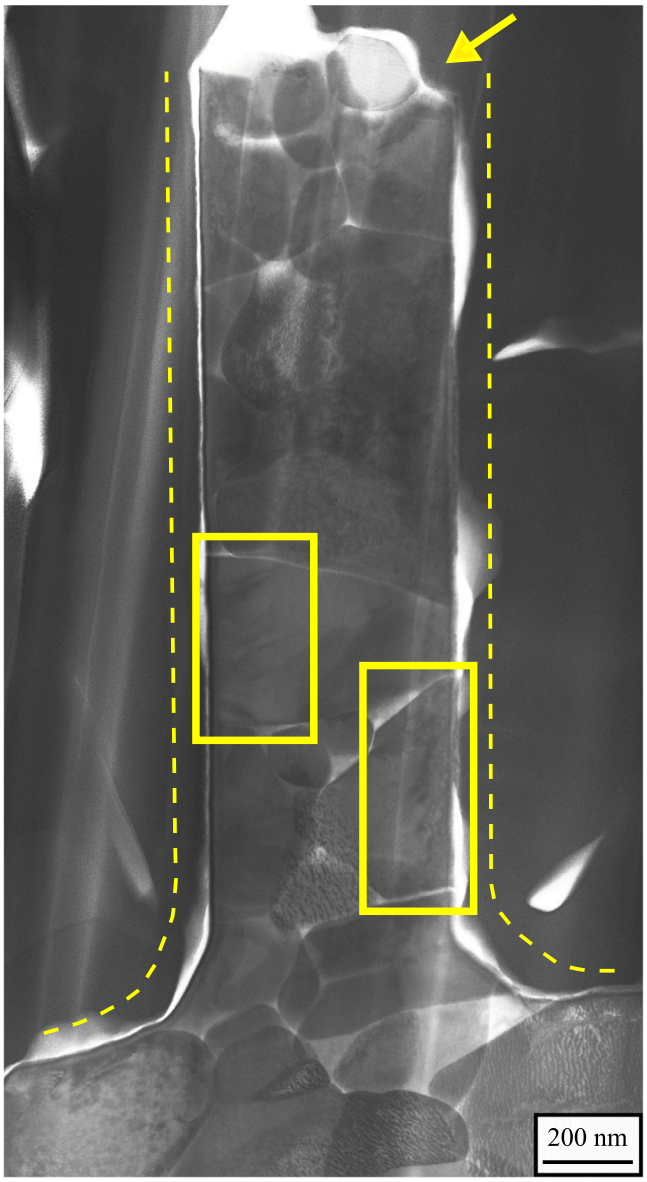


Fig. 7. STEM examination of the testing section after the micro tensile test. The loading direction was vertical. The contours of the testing section are marked with dashed lines with an intended offset and the fracture surface is indicated with an arrow. Two regions with increased dislocation density are marked with rectangles.

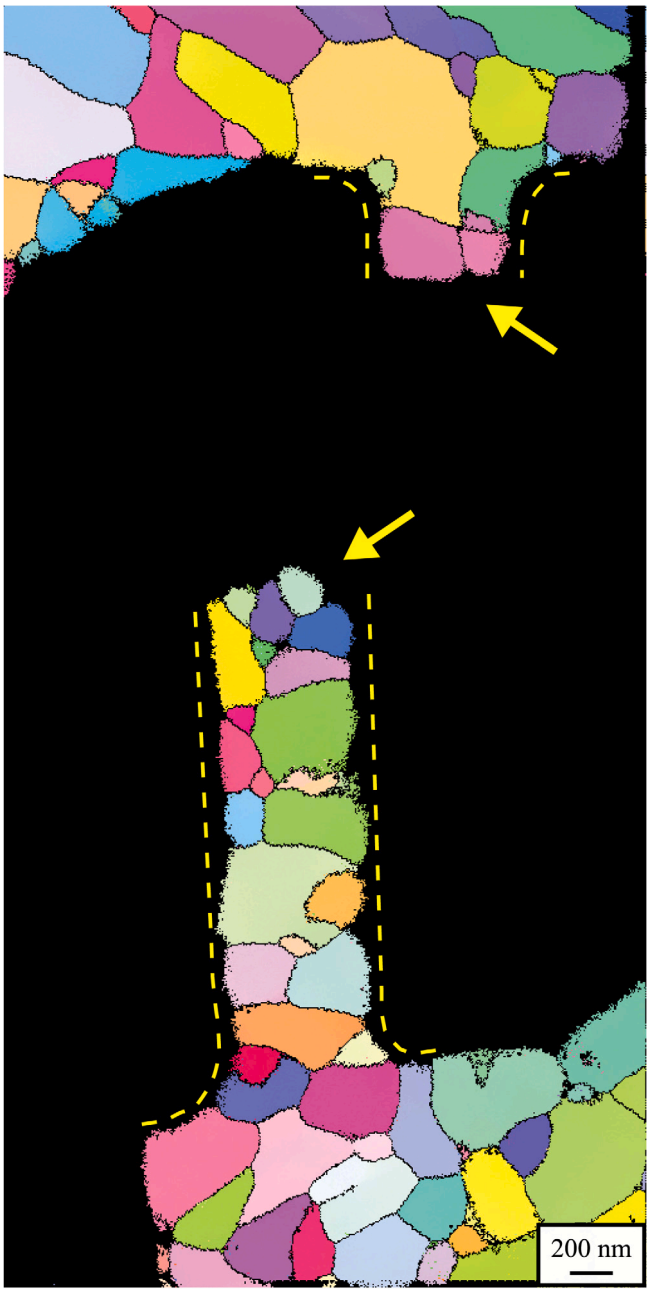


Fig. 8. TKD examination of the testing section after the micro tensile test. The loading direction was vertical. The contours of the testing section are marked with dashed lines with an intended offset and the fracture surfaces are indicated with arrows.

in the testing section and in particular on the fracture surface and assuming that the fracture surface is normal to the loading direction, the measured fracture stress is the average grain boundary strength over the grain boundaries on the fracture surface. Under the assumption of plane stress, the grain boundary stiffness can be estimated based on the fracture toughness K_I^{crit} and the Young's modulus E through the calculation of the critical energy release rate G^{crit} in Eq. (3) [48].

$$G^{crit} = \frac{K_I^{crit\,2}}{E} \tag{3}$$

Using $K_I^{crit} = 0.271\,\mathrm{MPa}\sqrt{\mathrm{m}}$ [23] and $E = 138\,\mathrm{GPa}$ from nanoindentation, the critical energy release rate becomes $G^{crit} = 0.53\,\mathrm{J\,m^{-2}}$ which is in good agreement with an estimation made by Han et al. [39] ($0.46\,\mathrm{J\,m^{-2}}$ to $0.69\,\mathrm{J\,m^{-2}}$). The critical energy release rate is equal to the integral of the stress–displacement (σ–δ) curve [39] of the grain boundary where the displacement can be replaced by the grain boundary stiffness $S_{gb} = \frac{\sigma}{\delta}$. For linear elastic material behavior and brittle fracture this results in Eq. (4).

$$G^{crit} = \int \sigma(\delta)\,\mathrm{d}\delta = \frac{1}{2}\sigma\delta = \frac{\sigma^2}{2S_{gb}} \tag{4}$$

With $\sigma = \sigma_{ch} = 745\,\mathrm{MPa}$, the resulting grain boundary stiffness is $S_{gb} = 521\,\mathrm{GPa/\mu m}$. This value can for example be used in cohesive elements in simulation models when the grain boundary thickness is known.

In this study, lithiated NMC was examined. Under the hypothesis that the lithium ions are stored in the crystal and not at the grain boundaries, it is assumed that the grain boundary strength varies little

with the lithiation state. Due to a weakening of the NMC crystal as a consequence of delithiation, the separate analysis of grain property changes and grain boundary property changes is however challenging.

This study focused on the examination of polycrystalline NMC and in particular the grain boundary strength which determines the intercrystalline crack formation. Recently, single crystalline NMC is gaining more attention. Through the inexistence of grain boundaries, one weak spot of the material is eliminated and the strength of the crystal itself becomes relevant since it determines the potential for transcrystalline crack growth. The single crystalline particles being small (of the order of 3 μm), the manufacturing of the here-developed specimen geometry is challenging. To determine the strength of the crystal and the transcrystalline crack formation behavior, smaller specimen geometries such as tensile specimens in combination with a dedicated push-to-pull device or micropillars for compression tests [44] are more suitable.

When performing mechanical tests on FIB produced samples on the micro scale, one important aspect is the amorphization of the sample surface through the ion beam. The STEM images and the TKD measurement showed that no relevant amorphization occurred during the sample preparation. Furthermore, the surface quality of the sample was good, in particular only slight longitudinal patterning was visible, but no transverse notches were present in the testing section.

The influence of the hinge on the measurement results is small. In some cases, the hinge fractured during the test, indicating an extremely thin material bridge between the sample and the substrate. In the cases where the hinge did not fracture during the test, the fractured sample was loaded again to measure the remaining stiffness only of the hinge. The indenter load taken by the hinge was smaller than 5 % of the fracture load of the corresponding tests, hence the error in the load measurement in the testing section is expected to be small.

The displacement was measured using digital image correlation. The theoretical resolution of the used Tescan Clara SEM is 0.9 nm, but the measured noise was approximately <3 nm for most samples. The measured maximum displacement being approximately 12 nm to 15 nm for most samples this results in the noise being approximately 20 % to 25 % of the maximum displacement. However, since the stress–strain curves are nearly perfectly linear and since the noise is random, the data could be post processed reliably with a Savitzky–Golay filter. An exemplary load–displacement curve with the raw data and the filtered data is presented in Supplementary material 5. This data is taken from a test where the field of view only captured the testing section. The measurement of the transverse strain was not possible because it was below the resolution of the SEM.

There are certain limitations to the chosen micro tensile testing approach. Firstly, during the specimen geometry optimization, a linear elastic material behavior was assumed. While this is a reasonable assumption for the here-examined NMC, the stress state in the testing section might deviate from the homogeneous and uniaxial stress state for materials that undergo plastic deformation. Furthermore, in order to avoid buckling or slipping of the indenter tip from the force application point, a certain minimum thickness of the specimen is required. Due to the small size of the specimen, the measurement probes highly local material properties which needs to be considered when effective or average material properties shall be determined. The specimen geometry is also not suitable for experimental examinations that require a large number of specimens for example for a robust statistical analysis, due to the time-consuming manufacturing and testing process.

5. Conclusion

Charging and discharging of batteries results in significant stresses in the electrode active material which finally fracture due to these mechanical loads. To understand and simulate the fracture behavior, both a qualitative and a quantitative knowledge of the material properties is required. In this study, polycrystalline NMC811 was examined under compressive and tensile loads. In both scenarios, intercrystalline fracture was observed. However, the less frequent occurrence of transcrystalline fracture was demonstrated in EBSD measurements. Furthermore, an optimized FIB produced push-to-pull sample geometry for micro tensile tests was developed. The stress–strain curve of NMC811 secondary particles was measured using this sample geometry and a digital image correlation technique for the displacement measurement. The method was validated against nanoindentation tests. The secondary particle Young's modulus, as well as the fracture stress and strain were measured using the micro tensile tests. A brittle fracture behavior was observed. From the results, the grain boundary strength and the grain boundary stiffness were derived. Both values can serve as quantitative measures for the robustness of the specific NMC species against mechanical loads as they occur during the service life of batteries. Their optimization and in particular a higher grain boundary strength minimizes degradation mechanisms through intercrystalline crack growth in polycrystalline NMC. The method can also be used to investigate interfaces in other materials.

CRediT authorship contribution statement

Tobias Sedlatschek: Writing – review & editing, Writing – original draft, Visualization, Methodology, Investigation, Formal analysis, Conceptualization. **Leonhard Gertlowski:** Writing – review & editing, Methodology. **Felix Weber:** Writing – review & editing, Supervision. **Christoph Broeckmann:** Supervision, Project administration, Funding acquisition.

Funding

This research did not receive any specific grant from funding agencies in the public, commercial, or not-for-profit sectors.

Declaration of competing interest

The authors declare that they have no known competing financial interests or personal relationships that could have appeared to influence the work reported in this paper.

Acknowledgments

The authors thank Changrun Wu for the optimization of the sample geometry and Xiaoyang Zheng for experimental assistance. Thank also goes to Alexander Schwedt for ion polishing and Lina Schwering for help with the nanoindentation. Furthermore, the authors thank Siyang Wang for providing the master pattern for the spherical indexing and Kai Donnerbauer for the EBSD analysis. Finally, thank goes to Malte Schmachtenberg for many FIB sessions.

Appendix A. Supplementary data

- 1-sample-geometry: Undeformed optimized sample geometry for micro tensile tests.
- 2-compression-test-A: Video of the cross-section of secondary particle A during a simple compression test.
- 3-compression-test-B: Video of the cross-section of secondary particle B during a simple compression test.
- 4-tensile-test: Video of the testing section in a secondary particle during a micro tensile test.
- 5-load–displacement-curve: Raw data of a representative micro tensile test.

Supplementary material related to this article can be found online at https://doi.org/10.1016/j.jpowsour.2026.240276.

Data availability

Data will be made available on request.

References

[1] R. Xiong, Y. Pan, W. Shen, H. Li, F. Sun, Lithium-ion battery aging mechanisms and diagnosis method for automotive applications: Recent advances and perspectives, Renew. Sustain. Energy Rev. 131 (110048) (2020) http://dx.doi.org/10.1016/j.rser.2020.110048.

[2] J. Hu, L. Li, E. Hu, S. Chae, H. Jia, T. Liu, B. Wu, Y. Bi, K. Amine, C. Wang, J. Zhang, J. Tao, J. Xiao, Mesoscale-architecture-based crack evolution dictating cycling stability of advanced lithium ion batteries, Nano Energy 79 (2021) http://dx.doi.org/10.1016/j.nanoen.2020.105420.

[3] N. Anderson, B. Zhang, A. Meng, X. Zhang, K. Lijesh, M. Khonsari, W. Meng, Cr-containing diamond-like carbon coatings deposited on 316 stainless steel substrates: Characterization and interfacial fracture toughness measurements, Surf. Coat. Technol. 462 (129462) (2023) http://dx.doi.org/10.1016/j.surfcoat.2023.129462.

[4] E. Okotete, S. Brinckmann, S. Lee, C. Kirchlechner, How to avoid FIB-milling artefacts in micro fracture? A new geometry for interface fracture, Mater. Des. 232 (112134) (2023) http://dx.doi.org/10.1016/j.matdes.2023.112134.

[5] Y. Ganesan, C. Peng, Y. Lu, L. Ci, A. Srivastava, P.M. Ajayan, J. Lou, Effect of nitrogen doping on the mechanical properties of carbon nanotubes, ACS Nano 4 (12) (2010) 7637–7643, http://dx.doi.org/10.1021/nn102372w.

[6] J. Lou, Y. Ganesan, Y. Lu, C. Peng, Micromechanical Devices for Materials Characterization, Patent US 8,058,613 B2, 2011.

[7] Y. Oh, E. Cyrankowski, Z. Shan, S.A.S. Asif, Micro/nano-Mechanical Test System Employing Tensile Test Holder with Push-To-Pull Transformer, Patent US 8,434,370 B2, 2013.

[8] A.J. Durelli, S. Morse, V. Parks, The theta specimen for determining tensile strength of brittle materials, Mater. Res. Stand. 2 (1962) 114.

[9] G.D. Quinn, E. Fuller, D. Xiang, A. Jillavenkatesa, L. Ma, D. Smith, J. Beall, A novel test method for measuring mechanical properties at the small-scale: the theta specimen, Ceram. Eng. Sci. Proc. 26 (2) (2005) 117–126, http://dx.doi.org/10.1002/9780470291221.ch15.

[10] M.-S. Ding, L. Tian, W.-Z. Han, J. Li, E. Ma, Z.-W. Shan, Nanobubble fragmentation and bubble-free-channel shear localization in helium-irradiated submicron-sized copper, Phys. Rev. Lett. 117 (2016) http://dx.doi.org/10.1103/PhysRevLett.117.215501.

[11] D. Kiener, C. Motz, G. Dehm, R. Pippan, Overview on established and novel FIB based miniaturized mechanical testing using in-situ SEM, Int. J. Mater. Res. 100 (8) (2009) 1074–1078, http://dx.doi.org/10.3139/146.110149.

[12] J.J. Schwiedrzik, J. Ast, L. Pethö, X. Maeder, J. Michler, A new push-pull sample design for microscale mode 1 fracture toughness measurements under uniaxial tension, Fatigue Fract. Eng. Mater. Struct. 41 (5) (2018) 991–1001, http://dx.doi.org/10.1111/ffe.12741.

[13] Y. Wang, L. Gao, S. Fan, W. Zhou, X. Li, Y. Lu, 3D printed micro-mechanical device (MMD) for in situ tensile testing of micro/nanowires, Extrem. Mech. Lett. 33 (2019) http://dx.doi.org/10.1016/j.eml.2019.100575.

[14] B. Shin, B. Ni, C.-T. Toh, D. Steinbach, Z. Yang, L.M. Sassi, Q. Ai, K. Niu, J. Lin, K. Suenaga, Y. Han, M.J. Buehler, B. Özyilmaz, J. Lou, Intrinsic toughening in monolayer amorphous carbon nanocomposites, Matter 8 (4) (2025) http://dx.doi.org/10.1016/j.matt.2025.102000.

[15] J. Varillas, J. Lukeš, A. Manikas, J. Mařák, J. Dluhoš, Z. Melníková, M. Kalbáč, C. Galiotis, O. Frank, Mechanical response of monolayer graphene via a multi-probe approach, Int. J. Mech. Sci. 273 (2024) http://dx.doi.org/10.1016/j.ijmecsci.2024.109208.

[16] E.R. Fuller, G.D. Quinn, R.F. Cook, Strength and fracture measurements at the nano scale, AIP Conf. Proc. 931 (2007) 156–160, http://dx.doi.org/10.1063/1.2799362.

[17] E.R. Fuller, D.L. Henann, L. Ma, Theta-like specimens for measuring mechanical properties at the small-scale: effects of non-ideal loading, Int. J. Mater. Res. 98 (8) (2007) http://dx.doi.org/10.3139/146.101527.

[18] J. Bauer, A. Schroer, R. Schwaiger, I. Tesari, C. Lange, L. Valdevit, O. Kraft, Push-to-pull tensile testing of ultra-strong nanoscale ceramic–polymer composites made by additive manufacturing, Extrem. Mech. Lett. 3 (2015) 105–112, http://dx.doi.org/10.1016/j.eml.2015.03.006.

[19] A. Jelinek, S. Zak, M.J. Cordill, D. Kiener, M. Alfreider, Nanoscale printed tunable specimen geometry enables high-throughput miniaturized fracture testing, Mater. Des. 234 (2023) http://dx.doi.org/10.1016/j.matdes.2023.112329.

[20] A.D. Smith, J. Donoghue, A. Garner, B. Winiarski, E. Bousser, J. Carr, J. Behnsen, T.L. Burnett, R. Wheeler, K. Wilford, P.J. Withers, M. Preuss, On the application of Xe^+ plasma FIB for micro-fabrication of small-scale tensile specimens, Exp. Mech. 59 (2019) 1113–1125, http://dx.doi.org/10.1007/s11340-019-00528-w.

[21] D. Du, H. Zhang, D.J. Srolovitz, Properties and determination of the interface stiffness, Acta Mater. 55 (2007) 467–471, http://dx.doi.org/10.1016/j.actamat.2006.08.038.

[22] K. Min, E. Cho, Intrinsic origin of intra-granular cracking in Ni-rich layered oxide cathode materials, Phys. Chem. Chem. Phys. 20 (9045) (2018) http://dx.doi.org/10.1039/c7cp06615e.

[23] N. Sharma, D. Meng, X. Wu, L.S. de Vasconcelos, L. Li, K. Zhao, Nanoindentation measurements of anisotropic mechanical properties of single crystalline NMC cathodes for li-ion batteries, Extrem. Mech. Lett. 58 (2023) http://dx.doi.org/10.1016/j.eml.2022.101920.

[24] H. Sun, K. Zhao, Electronic structure and comparative properties of $LiNi_xMn_yCo_zO_2$ cathode materials, J. Phys. Chem. C 121 (2017) 6002–6010, http://dx.doi.org/10.1021/acs.jpcc.7b00810.

[25] X. He, X. Ding, R. Xu, Anisotropic mechanical properties of $LiNi_xMn_yCo_{1-x-y}O_2$ cathodes for li-ion batteries: A first-principles theoretical study, Acta Mater. 267 (2024) http://dx.doi.org/10.1016/j.actamat.2024.119751.

[26] J. Liu, W. Lin, Z. Wang, Y. Wang, T. Chen, J. Zheng, Elastic mechanics study of layered $Li(Ni_xMn_yCo_z)O_2$, Phys. Rev. Journals Energy 3 (2024) http://dx.doi.org/10.1103/PRXEnergy.3.013012.

[27] L.S. de Vasconcelos, N. Sharma, R. Xu, K. Zhao, In-situ nanoindentation measurement of local mechanical behavior of a li-ion battery cathode in liquid electrolyte, Exp. Mech. 59 (2019) 337–347, http://dx.doi.org/10.1007/s11340-018-00451-6.

[28] L.S. de Vasconcelos, R. Xu, J. Li, K. Zhao, Grid indentation analysis of mechanical properties of composite electrodes in li-ion batteries, Extrem. Mech. Lett. 9 (2016) 495–502, http://dx.doi.org/10.1016/j.eml.2016.03.002.

[29] R. Xu, H. Sun, L.S. de Vasconcelos, K. Zhao, Mechanical and structural degradation of $LiNi_xMn_yCo_zO_2$ cathode in li-ion batteries: An experimental study, J. Electrochem. Soc. 164 (13) (2017) A3333–A3341, http://dx.doi.org/10.1149/2.1751713jes.

[30] J.C. Stallard, L. Wheatcroft, S.G. Booth, R. Boston, S.A. Corr, M.F.D. Volder, B.J. Inkson, N.A. Fleck, Mechanical properties of cathode materials for lithium-ion batteries, Joule 6 (5) (2022) 984–1007, http://dx.doi.org/10.1016/j.joule.2022.04.001.

[31] H.-R. Kim, S.-G. Woo, J.-H. Kim, W. Cho, Y.-J. Kim, Capacity fading behavior of Ni-rich layered cathode materials in li-ion full cells, J. Electroanal. Chem. 782 (2016) 168–173, http://dx.doi.org/10.1016/j.jelechem.2016.10.032.

[32] D. Dang, Y. Wang, Y.-T. Cheng, Fracture behavior of single $LiNi_{0.33}Mn_{0.33}Co_{0.33}O_2$ particles studied by flat punch indentation, J. Electrochem. Soc. 166 (13) (2019) A2749–A2751, http://dx.doi.org/10.1149/2.0331913jes.

[33] S. Maeng, Y. Chung, S. Min, Y. Shin, Enhanced mechanical strength and electrochemical performance of core–shell structured high–nickel cathode material, J. Power Sources 448 (2020) http://dx.doi.org/10.1016/j.jpowsour.2019.227395.

[34] G.-T. Park, D.R. Yoon, U.-H. Kim, B. Namkoong, J. Lee, M.M. Wang, A.C. Lee, X.W. Gu, W.C. Chueh, C.S. Yoon, Y.-K. Sun, Ultrafine-grained Ni-rich layered cathode for advanced li-ion batteries, Energy & Environ. Sci. 14 (2021) 6616–6626, http://dx.doi.org/10.1039/d1ee02898g.

[35] P. Ju, L. Ben, Y. Li, H. Yu, W. Zhao, Y. Chen, Y. Zhu, X. Huang, Designer particle morphology to eliminate local strain accumulation in high-nickel layered cathode materials, ACS Energy Lett. 8 (9) (2023) 3800–3810, http://dx.doi.org/10.1021/acsenergylett.3c01272.

[36] G.-T. Park, S.-M. Han, J.-H. Ryu, M.-C. Kim, D.-H. Kim, M.-S. Kim, Y.-K. Sun, Opening a new horizon for the facile synthesis of long-life Ni-rich layered cathode, ACS Energy Lett. 8 (9) (2023) 3784–3792, http://dx.doi.org/10.1021/acsenergylett.3c01322.

[37] H.-H. Ryu, H.-W. Lim, S.G. Lee, Y.-K. Sun, Optimization of molybdenum-doped Ni-rich layered cathodes for long-term cycling, Energy Storage Mater. 59 (102771) (2023) http://dx.doi.org/10.1016/j.ensm.2023.102771.

[38] L. Wheatcroft, A. Bird, J.C. Stallard, R.L. Mitchell, S.G. Booth, A.J. Nedoma, M.F.L.D. Volder, S.A. Cussen, N.A. Fleck, B.J. Inkson, Fracture testing of lithium-ion battery cathode secondary particles in-situ inside the scanning electron microscope, Batter. & Supercaps 6 (5) (2023) http://dx.doi.org/10.1002/batt.202300032.

[39] J. Han, R. Ghosh, F. Lin, K. Zhao, Microstructure informed mechanical properties and chemomechanical degradation of battery cathode particles, Exp. Mech. (2025) http://dx.doi.org/10.1007/s11340-025-01222-w.

[40] C.A. Schneider, W.S. Rasband, K.W. Eliceiri, NIH image to imagej: 25 years of image analysis, Nature Methods 9 (2012) 671–675, http://dx.doi.org/10.1038/nmeth.2089.

[41] W.C. Oliver, G.M. Pharr, An improved technique for determining hardness and elastic modulus using load and displacement sensing indentation experiments, J. Mater. Res. 7 (6) (1992) 1564–1583, http://dx.doi.org/10.1557/JMR.1992.1564.

[42] T. Sedlatschek, M. Krämer, J.S.-L. Gibson, S. Korte-Kerzel, A. Bezold, C. Broeckmann, Mechanical properties of heterogeneous, porous $LiFePO_4$ cathodes obtained using statistical nanoindentation and micromechanical simulations, J. Power Sources 539 (2022) http://dx.doi.org/10.1016/j.jpowsour.2022.231565.

[43] J.-M. Lim, H. Kim, K. Cho, M. Cho, Fundamental mechanisms of fracture and its suppression in Ni-rich layered cathodes: Mechanics-based multiscale approaches, Extrem. Mech. Lett. 22 (2018) 98–105, http://dx.doi.org/10.1016/j.eml.2018.05.010.

[44] S. Wang, Z. Shen, A. Omirkhan, O. Gavalda-Diaz, M.P. Ryan, F. Giuliani, Determining the fundamental failure modes in Ni-rich lithium ion battery cathodes, J. Eur. Ceram. Soc. 43 (16) (2023) 7553–7560, http://dx.doi.org/10.1016/j.jeurceramsoc.2023.08.021.

[45] A. Wade, A.V. Llewellyn, T.M.M. Heenan, C. Tan, D.J.L. Brett, R. Jervis, P.R. Shearing, First cycle cracking behaviour within Ni-rich cathodes during high-voltage charging, J. Electrochem. Soc. 170 (7) (2023) 070513, http://dx.doi.org/10.1149/1945-7111/ace130.

[46] A.H. Iyer, P. Gupta, P. Gudmundson, A. Kulachenko, Measuring microscale mechanical properties of pvdf binder phase and the binder-particle interface using micromechanical testing, Mater. Sci. Eng. A 881 (2023) http://dx.doi.org/10.1016/j.msea.2023.145352.

[47] C. Xu, Z. Ahmad, A. Aryanfar, V. Viswanathan, J.R. Greer, Enhanced strength and temperature dependence of mechanical properties of li at small scales and its implications for li metal anodes, PNAS 114 (1) (2016) 57–61, http://dx.doi.org/10.1073/pnas.1615733114.

[48] G.R. Irwin, Fracturing and fracture mechanics, 1961, URL http://hdl.handle.net/2142/111915.